Check for updates

Flexible Fe₃Si/SiC ultrathin hybrid fiber mats with designable microwave absorption performance†

Yi Hou, [iD] [a] Yani Zhang,*[a] Xiaoqing Du,[a] Yong Yang,[b] Chaoran Deng,[b] Zhihong Yang,[c] Lianxi Zheng [iD] [d] and Laifei Cheng*[a]

Flexible Fe₃Si/SiC ultrathin fiber mats have been fabricated by electrospinning and high temperature treatment (1400 °C) using polycarbosilane (PCS) and ferric acetylacetonate (Fe(acac)₃) as precursors. The crystallization degree, flexibility, electrical conductivity, dielectric loss and microwave absorption properties of the hybrid fibers have been dramatically enhanced by the introduction of Fe. Fe₃Si nanoparticles with a diameter around 500 nm are embedded in SiC fibers. As the Fe₃Si content increases from 0 to 6.5 wt%, the related saturation magnetization (M_s) values increase from 0 to 8.4 emu g^{-1}, and the electrical conductivity rises from 7.9×10^{-8} to 3.1×10^{-3} S cm^{-1}. Moreover, the flexibility of Fe₃Si/SiC hybrid fiber mats is greatly improved and remains intact after 500 times 180°-bending testing. Compared with pure SiC fibers, the Fe₃Si/SiC hybrid fibers process higher dielectric and magnetic loss, which would be further advanced as more Fe₃Si phase is introduced. At the optimal Fe₃Si content of 3.8 wt%, the Fe₃Si/SiC fibers/silicon resin composite (5 wt%) exhibits minimal reflection loss (RL) of −22.5 dB at 16.5 GHz and 2.5 mm thickness with a wide effective absorption bandwidth (EAB, RL < −10 dB) of 8.5 GHz. The microwave absorption performance can be further promoted by multi component stacking fiber mat composites which contain both low and high Fe₃Si content layers. Furthermore, the position of the microwave absorption bands can also be simply manipulated by designing the stacking components and structure.

1 Introduction

With ideal mechanical properties, excellent chemical stability, outstanding high temperature resistance and low density,[1–5] silicon carbide (SiC) has been recognized as an ideal candidate for both structural (e.g., composites reinforcement/matrix,[6,7] aero-engine,[3,8] nuclear reactor,[9–11] etc.) and functional materials (e.g., electromagnetic wave (EM) absorbers,[12,13] catalyst templates,[14,15] mechanical/gas sensors supporters,[16] etc.) operating in harsh environments. In particular, SiC is a suitable EM absorber material due to its wide band gap, tunable electrical conductivity and dielectric properties,[2,13] exhibiting the appropriate impedance match to realize good EM attenuation ability. Moreover, 1D SiC nano-materials (such as SiC nanofibers, whiskers or nanowires), with high surface area and designable microstructure, have been proved to provide superior EM absorption capacity to bulk or particle SiC materials.[17,18]

Compared with carbon and ferromagnetic EM absorbers, pure SiC phase shows relatively lower dielectric loss ability. Therefore, defects[18,19] or second phase additions (e.g. nano-carbon phase,[20–24] ZnO nano-crystals,[25] Al doping[26]) are usually introduced to enhance the permittivity of 1D SiC nano-materials, achieving a proper impedance match degree for microwave absorption properties. In particular, magnetic phase doped 1D SiC nano-materials, such as Fe–SiC whisker,[19] Fe₃O₄–SiC hybrid nanowires,[27] and Co–SiC hybrid nanowires,[28] could effectively improve the EM absorption performance by introducing both dielectric and magnetic losses. Recently, we have successfully fabricated Fe/SiC hybrid fiber with outstanding EM absorption properties.[29] However, the as-prepared Fe/SiC hybrid fiber mat presented large diameter (5–10 μm) and weak flexibility, which would greatly limit its practical application. On the other hand, the fibers' continuity and distribution have been proved to be highly significant for the dielectric and microwave absorption performance of the SiC nanofiber mat.[30] To the best of our knowledge, the influence of components and structure design on the EM absorption properties for flexible magnetic phase/SiC fiber mat has not been investigated.

[a]Science and Technology on Thermostructural Composite Materials Laboratory, Northwestern Polytechnical University, 710072, Xi'an, China. E-mail: chenglf@nwpu.edu.cn; zhangyani@nwpu.edu.cn

[b]Temasek Laboratories, National University of Singapore, 5A Engineering Drive 1, 117411, Singapore

[c]College of Material Science and Technology, Nanjing University of Aeronautics and Astronautics, 210016, Nanjing, China

[d]Department of Mechanical Engineering, Khalifa University, 127788, Abu Dhabi, United Arab Emirates

† Electronic supplementary information (ESI) available. See DOI: 10.1039/c8ra06941g

Compared with the aforementioned magnetic phases, Fe–Si alloy, as one kind of magnetic alloys, shows high Curie point and oxidation resistance.[31] Therefore, the composition of Fe–Si alloy into SiC fibers could be an effective approach to improve the EM absorption properties without sacrificing the high temperature stability. In this work, flexible Fe_3Si/SiC ultrathin fiber mats with different Fe_3Si contents were successfully prepared by electrospinning, which has been widely adopted to fabricate 1D nano-materials (nanofibers, nano-nets and nano-rods) with controllable microstructure, morphology, and distribution.[2,32–34] For the electrospinning solution, poly-carbosilane (PCS) is accepted as the precursor of continuous SiC fibers. Additionally, ferric acetylacetonate ($Fe(acac)_3$), with good solubility in the PCS solution, was applied as the additive of Fe element to overcome the brittleness of Fe/SiC hybrid fiber. The morphology, phase composition, flexibility, EM parameters, microwave absorption properties of Fe_3Si/SiC ultrathin fibers with different Fe_3Si contents were systematically investigated. Furthermore, we also explored a new structure designing method to manipulate the microwave absorption properties by stacking design of multi components Fe_3Si/SiC fibers composites.

2 Experimental

2.1. Fabrication of Fe_3Si/SiC ultrathin fiber mats

The fabrication process of Fe_3Si/SiC ultrathin fiber mats is illustrated in Fig. 1. The first step is to prepare SiC precursor solution, in which PCS (average Mn 2000) and $Fe(acac)_3$ are used as the precursors of SiC and Fe_3Si, respectively. 3 g PCS and different mass of $Fe(acac)_3$ are mixed with 1 g poly-caprolactone (PCL, average Mn 80 000) and then dispersed into 20 mL chloroform. The detailed precursor solution parameters are shown in Table 1. The mixture was stirred for 24 h to form homogeneous $Fe(acac)_3$/PCS solution. Secondly, the solution was pumped into a plastic syringe (20 mL) with a metal needle

Table 1 Precursor solution parameters of the Fe_3Si/SiC hybrid fiber mats

Sample names	PCS (g)	PCL (g)	$Fe(acac)_3$ (g)	Fe_3Si content in Fe_3Si/SiC fiber (wt%)
Pure SiC	3	1	0	0
Fe_3Si-1.6 wt%	3	1	0.25	1.6
Fe_3Si-3.8 wt%	3	1	0.75	3.8
Fe_3Si-6.5 wt%	3	1	1	6.5

(inner diameter: 0.51 mm) and placed in the electrospinning device. In the electrospinning process, the positive voltage between the needle and the collector was 25 kV. The pumping speed of the syringe was 2 mL h^{-1}. Then the as-spun fiber mat was peeled off from the roller collector and put into an oven for curing treatment at 200 °C lasting 2 h. At last, the cured fiber mat was pyrolyzed at 1400 °C for 2 h in Ar protecting atmosphere.

2.2. Characterization

The morphology of Fe_3Si/SiC fibers was observe by a scanning electron microscope (SEM, S-4700, Hitachi, 15 kV). X-ray diffraction (XRD, Rigaku Ultima IV with Cu Kα radiation) as well as transmission electron microscopy (TEM, F-30 FEI-Tecnai, 300 kV) were used to characterize the crystalline and phase structure. Static electrical conductivity was tested by four-probe method with a current source (Keithley 6220 DC; Ohio, USA). Dynamic electrical conductivity test under 180°-bending cycles were carried out using a direct current (DC) resistance tester (Zhi Xin ZX5512, Changzhou, China). For permittivity and permeability measurement, Fe_3Si/SiC fiber mats/silicon resin composite (5 wt% fiber mats) were prepared using our self-made tamping die mold.[30] The composite samples were made into toroid-shaped shape (D_{out}: 7 mm, D_{in}: 3 mm) and then
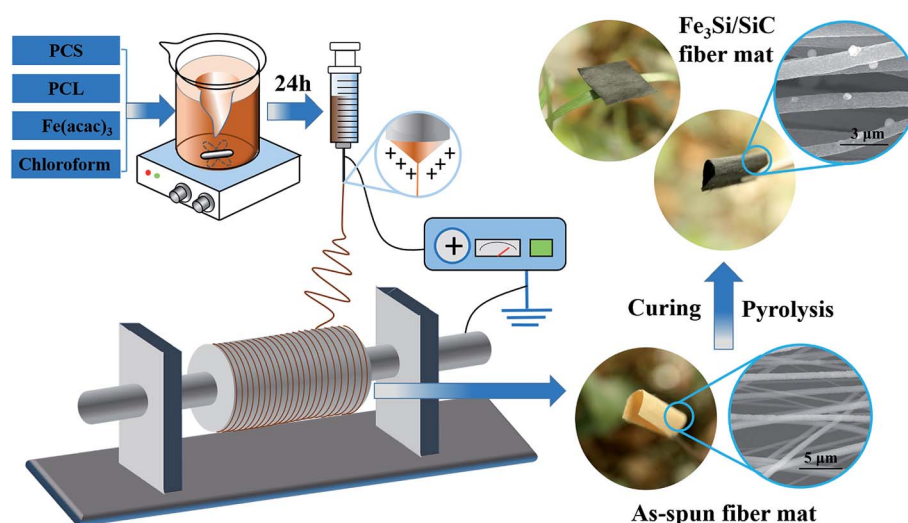

Fig. 1 Schematic diagram of the preparing process of Fe_3Si/SiC ultrathin fiber mats. The insets at the bottom and top right corners are the digital photos and local enlarged SEM images of as-spun fiber mat and Fe_3Si/SiC fiber mat, separately.

placed in the coaxial line mode of Agilent vector network analyser HP8722D to measure and calculate complex permittivity ($\varepsilon_r = \varepsilon' - j\varepsilon''$) and permeability ($\mu_r = \mu' - j\mu''$).

Based on transmission-line theory and metal back-panel model,[35–37] the reflection loss (RL) values were calculated by ε_r and μ_r to evaluate the microwave absorption properties.

$$RL = 20 \log_{10}|(Z_{in} - Z_0)/(Z_{in} + Z_0)| \qquad (1)$$

$$Z_0 = (\mu_0/\varepsilon_0)^{1/2} \qquad (2)$$

$$Z_{in} = Z_0 (\mu_r/\varepsilon_r)^{1/2} \tanh[j(2\pi fd/c)(\mu_r\varepsilon_r)^{1/2}] \qquad (3)$$

where Z_{in} means the impedance of the composite backed by the ground plane, Z_0 is the intrinsic impedance of free space, f is the frequency of incident EM waves, d is the thickness of absorber, c is the speed of light.

3   Results and discussion

3.1.   Microstructure and chemical composition

The diameter of pure SiC fibers is around 5 μm (as shown in Fig. S1†). As the introducing of Fe$_3$Si phase, the diameter of Fe$_3$Si/SiC hybrid fibers (Fig. 2(a)–(f)) greatly drops to 1–2 μm. The reduction of fiber size is mainly contributed from the adding of Fe(acac)$_3$ in the PCS solution, which enhances the electrical conductivity and spinnability of the precursor solution. In the process of electrospinning, a jet of the pendant droplet at the tip of needle becomes highly electrified when the high voltage is applied. And the droplet will form into a conical shape called Taylor cone, from which a liquid jet will be ejected out once the electric energy surpasses the surface free energy of the electrospun solution. With the introduction of Fe(acac)$_3$, there would be a larger charge density on the surface of Taylor cone, so more electric charges could be loaded by the solution jet.[34,38] Such effect was also observed and reported in the electrospun polymer nanofibers with salts additive.[39,40] And the crystallization degree, flexibility and EM properties of Fe$_3$Si/SiC fibers will also be further influenced by the adding of Fe(acac)$_3$ and the reduction of fibers diameter, which would be discussed later. As the Fe$_3$Si content increased from 1.6 to 3.8 wt%, nanoparticles with the average size of 500 nm appear on the surface of Fe$_3$Si/SiC fibers (Fig. 2(c) and (d)). And the nanoparticles' number further rises when the Fe$_3$Si content increases to 6.5 wt% (Fig. 2(e) and (f)). According to the EDS element mapping images of an individual Fe$_3$Si-3.8 wt% fiber in Fig. 2(g) and (h), Si is uniformly distributed in the whole fiber while Fe is mainly concentrated in the nanoparticles, implying that the nanoparticles might be made of Fe$_3$Si phase, which will be elaborated in the following parts.

To further verify the crystal structure and phase distribution of Fe$_3$Si/SiC hybrid fibers, the transmission electron microscopy (TEM) images and selected area electron diffraction (SAED) patterns detected form different parts (A and B in Fig. 3(a)) were acquired and presented in Fig. 3(a)–(e). The high-resolution TEM (HRTEM) image of area A (Fig. 3(b)) reveals a distinguishable lattice spacing of 0.25 nm, matching the spacing of the
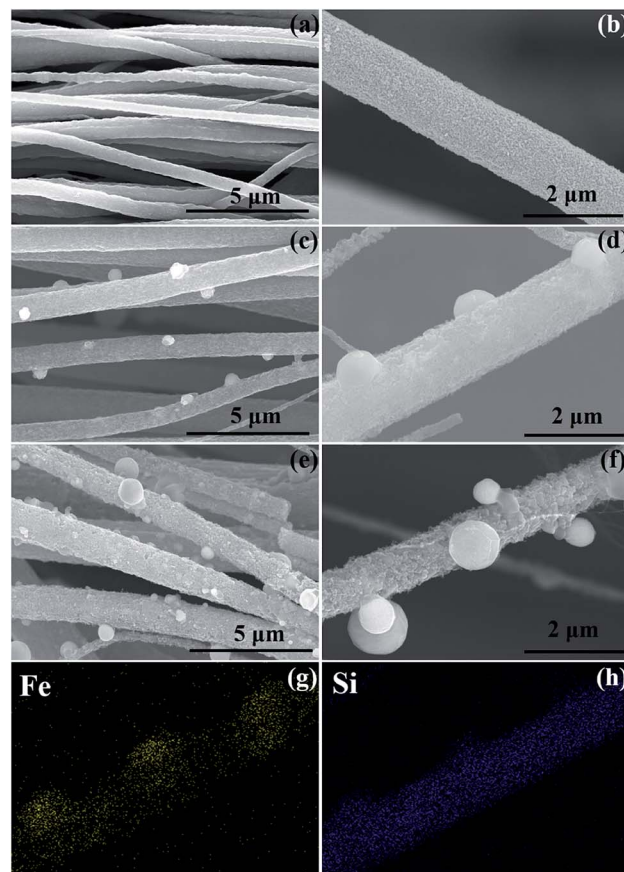

Fig. 2   (a)–(f) SEM images of Fe$_3$Si/SiC hybrid fibers with different Fe$_3$Si contents: (a and b) Fe$_3$Si-1.6 wt%; (c and d) Fe$_3$Si-3.8 wt%; (e and f) Fe$_3$Si-6.5 wt%. (g and h) EDS mapping images (Fe and Si) of Fe$_3$Si-3.8 wt% sample.

(111) plane of β-SiC.[15,41] Meanwhile, Fe$_3$Si phase, together with SiC phase was also detected in the SAED patterns of area A (Fig. 3(c)), which is formed from the adding of Fe(acac)$_3$ in the precursor during the pyrolysis process.

In the nanoparticle part, the lattice spacing of 0.20 nm in area B (Fig. 3(d)) agrees well with the (220) plane of Fe$_3$Si phase.[42,43] Carbon phase is usually existed in SiC ceramic fabricated by polymer-derived ceramic (PDC) and originated from the pyrolysis PCS precursor.[29] From Fig. 3(d) it is also found that a thin graphite layer with the thickness of 5–10 nm was coated on the surface of nanoparticles.[22] Moreover, SAED patterns in Fig. 3(e) further confirm the existence of Fe$_3$Si phase[44] and graphite.[45] However, SiC phase is not observed in area B from the results in Fig. 3(d) and (e). Therefore, it can be verified that Fe$_3$Si phase is mainly concentrated in the nanoparticles (area B). While in the fiber part (area A), SiC and Fe$_3$Si phase are coexisted.

The X-ray diffraction (XRD) patterns of pure SiC fibers and Fe$_3$Si/SiC hybrid fibers were compared and exhibited in Fig. 4(a). The diffraction peaks of β-SiC (JCPDS#74-2307; 35.6°, 60.0° and 71.8°)[21] are observed in all the patterns, which become much sharper as the Fe$_3$Si content increased from 0 to 6.5 wt%, implying that the crystalline size are getting larger.
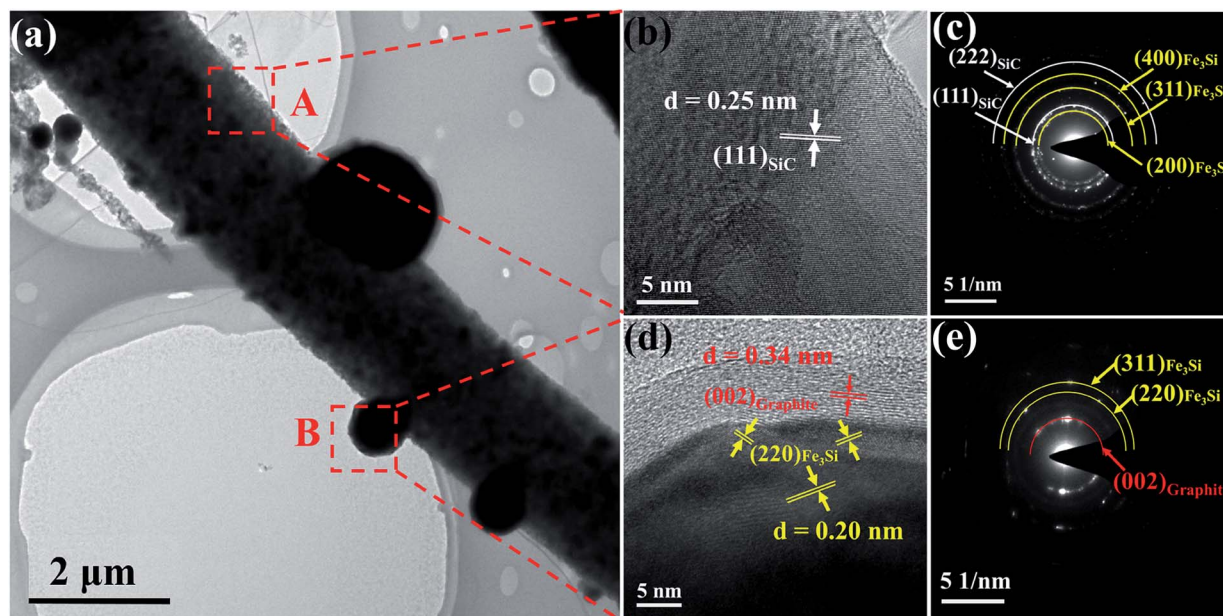
Fig. 3 (a) TEM image of a single Fe_3Si/SiC (Fe_3Si-3.8 wt%) fiber; HRTEM and SAED images of the (b and c) fiber part (area A) and (d and e) nanoparticle part (area B) of the hybrid fiber.

Actually, the adding of $Fe(acac)_3$ in the PCS solution can promote the formation of SiC phase, which is attributed to the Fe element acting as the catalyst when SiC crystal was formed from PCS precursor.[30,46] In addition, Fe_3Si phase is also detected with the peaks at 45.3°, 66.1° and 83.7° (JCPDS#45-1207)[47] for Fe_3Si/SiC hybrid fibers, corresponding to the HRTEM and SAED results in Fig. 3(c)–(e). The Fe_3Si phase was formed from $Fe(acac)_3$ in the heat treatment process. $Fe(acac)_3$ was converted to Fe_3O_4 at relatively low pyrolysis temperature (<800 °C) and reduced into Fe_3Si in Si-rich environment at high temperature (>800 °C). The conversion process was described in detail in our last article.[30] Fig. 4(b) shows the hysteresis loops of Fe_3Si/SiC hybrid fibers with different Fe_3Si contents, it can be seen that the hybrid fibers demonstrate ferromagnetic behaviour, resulting from the Fe_3Si phase with a half-metallic property.[42,48] For the sample of Fe_3Si-1.6/3.8/6.5 wt%, the related saturation

magnetization (M_s) values are 2.5/5.0/8.4 emu g^{-1}, separately. Meanwhile, the coercivity (H_c) of Fe_3Si-1.6 wt% and 6.5 wt% are about 50 Oe, while the H_c of Fe_3Si-3.8 wt% slightly grows to 90 Oe.

180° bending test was performed to evaluate the flexibility of Fe_3Si/SiC hybrid fiber mats. The testing sample of pure SiC fiber mat was broken in two pieces even at the first bending cycle (as shown in Fig. S2†), implying a very brittle feature. By comparison, the flexibility is drastically improved for Fe_3Si/SiC hybrid fiber mats. In the process of 500 times bending test, as shown in Fig. 5, the electric resistance changing ratio ($\Delta R/R_0$) of Fe_3Si-1.6 wt% and Fe_3Si-3.8 wt% remained below 1%, meaning the fibers kept intact in the whole testing process. Such enhanced flexibility is owing to the smaller fiber diameter and higher crystallization degree than pure SiC fibers.[31,49] However, as the Fe_3Si content further increased to 6.3 wt%, the $\Delta R/R_0$ value
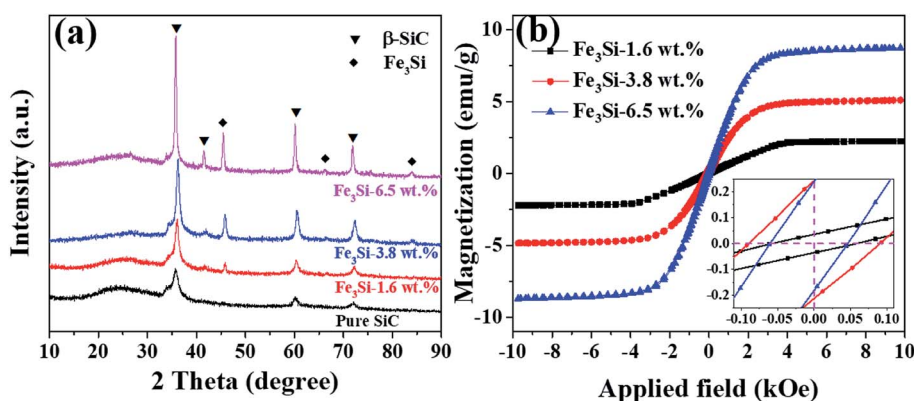

Fig. 4 (a) XRD patterns of pure SiC fibers and Fe_3Si/SiC hybrid fibers with different Fe_3Si; (b) room-temperature hysteresis loops of Fe_3Si/SiC hybrid fibers with different Fe_3Si contents.

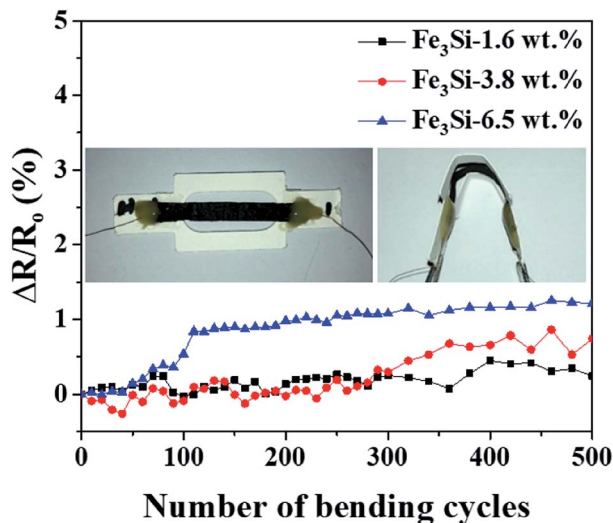**Fig. 5** Electrical resistance changing ratio ($\Delta R/R_0$) under cyclic bending deformations of Fe₃Si/SiC hybrid fibers with different Fe₃Si content.

obviously jumps above 1% after 100 times bending. The decline of flexibility attributes to the over loading to Fe₃Si nanoparticles, which may act as the crack initiation points and introduce more defects to the hybrid fibers.

3.2. EM and microwave absorption properties

The resin composites (5 wt%) for EM parameters testing contains 6 layers single/multi component stacking fiber mats, which were cut into toroidal-shape (D_{out}: 7.0 mm, D_{in}: 3.0 mm) testing samples by our self-made stamping die mould.[30]

3.2.1 Single component stacking fiber mats composites. The complex permittivity ($\varepsilon_r = \varepsilon' - j\varepsilon''$) of pure SiC and Fe₃Si/SiC fibers are presented in Fig. 6(a) and (b). It can be seen that pure SiC fibers sample shows the lowest ε' and ε'' values. As the Fe₃Si content increased from 1.6 to 6.5 wt%, the value of ε_r grows gradually, implying an enhanced polarization and dielectric loss ability. As shown in Fig. 2 and 3, the Fe₃Si nanoparticles in the Fe₃Si/SiC fibers would bring a large number of grain boundaries and interfaces between SiC and Fe₃Si, advancing the interfacial polarization capacity of hybrid fibers. On the other side, the electrical conductivity of hybrid fibers are further promoted because of the Fe₃Si phase with higher conductivity than SiC, which has been confirmed by the electrical conductivity testing results in Table 2. According to Debye theory,[50] the electrical conductivity of EM absorbers directly determines the value of ε'', Therefore, the introduction of more Fe₃Si content, with higher electrical conductivity, could lead to the rise of ε'' (as shown in Fig. 6(b)). Similar tendency is found in the value of permeability ($\mu_r = \mu' - j\mu''$), which also strongly depends on the
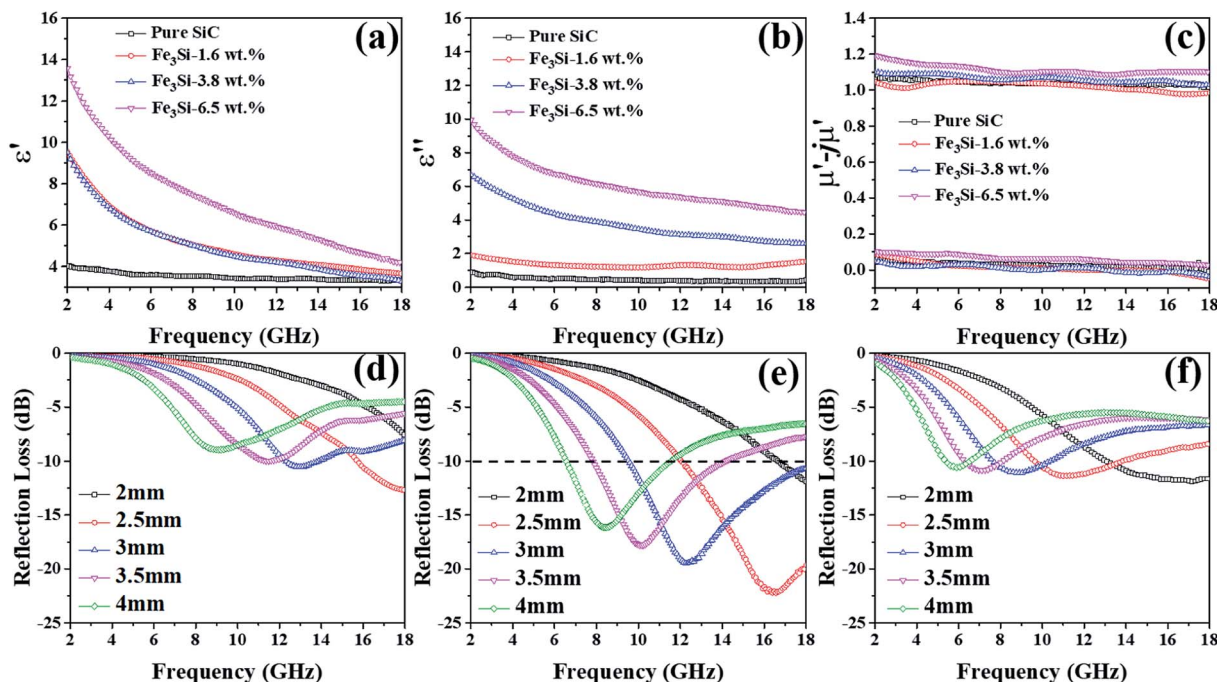

Fig. 6 Frequency dependent (a and b) complex permittivity ($\varepsilon_r = \varepsilon' - j\varepsilon''$) and (c) complex permeability ($\mu_r = \mu' - j\mu''$); calculated frequency dependent reflection loss (RL) of single component stacking Fe₃Si/SiC fibers/silicon resin composite (5 wt%) samples: (d) Fe₃Si-1.6 wt%, (e) Fe₃Si-3.8 wt% and (f) Fe₃Si-6.5 wt%.

Table 2 Electrical conductivity of pure SiC and Fe₃Si/SiC hybrid fiber mats

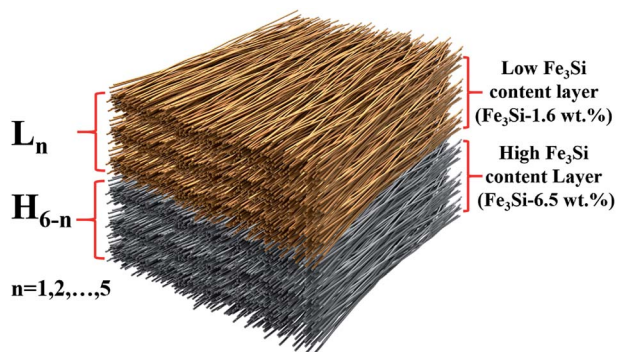| Sample names	Pure SiC	Fe₃Si-1.6 wt%	Fe₃Si-3.8 wt%	Fe₃Si-6.5 wt%
Conductivity(S cm⁻¹)	7.9×10^{-8}	3.1×10^{-5}	5.1×10^{-4}	3.1×10^{-3}

Fig. 7 Stacking design of multi components stacking fiber mats composites.

Fe$_3$Si content (Fig. 6(c)). Since SiC is a dielectric ceramic material, the magnetic resonance in μ_r is contributed by Fe$_3$Si phase.

The reflection loss (RL) of pure SiC and Fe$_3$Si/SiC fibers (depicted in Fig. S3† and 6(d)–(f)) are calculated to evaluate the microwave absorption capacity by using eqn (1)–(3). Pure SiC fibers sample (Fig. S3†) still shows the worst microwave absorption property and the RL values are above −5 dB with the sample thickness from 2–4 mm. For the sample of Fe$_3$Si-1.6 wt%, the situation is slightly modified as shown in Fig. 6(d), where the minimal RL value decreases to −12.8 dB at 18 GHz at 2.5 mm. As the Fe$_3$Si content is further increased to 3.8 wt%, a remarkable improvement of the RL values is shown up (Fig. 6(e)). At 16.5 GHz and 2.5 mm thickness, the RL value reaches −22.5 dB, associated with the effective absorption areas (EAB, RL < −10 dB, 90% absorption) as broad as 8.5 GHz (9.5–18 GHz at 3 mm thickness). However, over loading of Fe$_3$Si would lead to the decay of microwave absorption property. As illustrated in Fig. 6(f), the minimal RL value of Fe$_3$Si-6.3 wt% is only −11.9 dB at 17.0 GHz with the sample thickness of 2 mm. The drop of RL values should be blamed on the improper matched characteristic impedance. Based on the back-panel model and $\lambda/4$ cancellation theory, the maximum RL values would be realized when the phase difference between incident and reflected wave at the air-absorber (AA) interface is 180°.[51–53] Besides, the amplitudes of the two waves that related to ε_r and μ_r

have to be equal in order to achieve the optimal cancellation scenario. If the characteristic impedance matches well, more microwave would enter the absorbers and be dissipated. Otherwise the microwave would mostly be reflected in the surface of absorbers. The modulus of $Z_{in} − 1$ ($|Z_{in} − 1|$) that calculated by eqn (2) and (3) is used to evaluate the characteristic impedance matching degree. As shown in Fig. S4†, the $|Z_{in} − 1|$ value of pure SiC fibers is far away from 0 in the whole frequency range, meaning that the characteristic impedance is mismatched. As for the Fe$_3$Si/SiC hybrid fibers, the $|Z_{in} − 1|$ value of Fe$_3$Si-3.8 wt% sample gets closest to zero, then followed by Fe$_3$Si-6.5 wt% and Fe$_3$Si-1.6 wt% separately. As a result, Fe$_3$Si-3.8 wt% sample exhibits the best characteristic impedance matching degree and consequently has the lowest RL values. Moreover, it is worth noticing that introducing Fe$_3$Si phase into SiC fibers could apparently shift the RL peaks to lower frequency range, and the shifting degree is enhanced with the increasing content of Fe$_3$Si. Such effect should be ascribed to the magnetic loss that introduced by Fe$_3$Si phase, which has been confirmed and discussed in our last report.[29]

3.2.2 Multi components stacking fiber mats composites. The Fe$_3$Si/SiC hybrid fiber mats composites stacked by multi components fiber layers were also prepared to further enhance the RL values and then manipulate the microwave absorption parameters. As shown in Fig. 7, different numbers of low Fe$_3$Si content layers (Fe$_3$Si-1.6 wt%) and high Fe$_3$Si content layers (Fe$_3$Si-6.5 wt%) were stacked to form 6 layers' Fe$_3$Si/SiC fibers/silicon resin composite (5 wt%) samples.

The EM parameters of multi components stacking fiber mats composites were measured and presented in Fig. 8. With the number of high Fe$_3$Si content layer increased from 1–5, the polarization and dielectric loss ability of the stacking fiber mats composite would be gradually advanced, hence, both ε' and ε'' are slightly promoted in most frequency range (shown in Fig. 8(a) and (b)). It means that the permittivity of Fe$_3$Si/SiC fibers/silicon resin composites can be easily tuned by the stacking component designing. In addition, since the Fe$_3$Si content in our prepared Fe$_3$Si/SiC hybrid fibers is less than 7%, the magnetic loss would not play a dominated role in the EM properties of multi components stacking fiber mats composites, corresponding with the results in Fig. 8(c) that no obvious difference is found in the permeability ($\mu_r = \mu' − j\mu''$) curves.
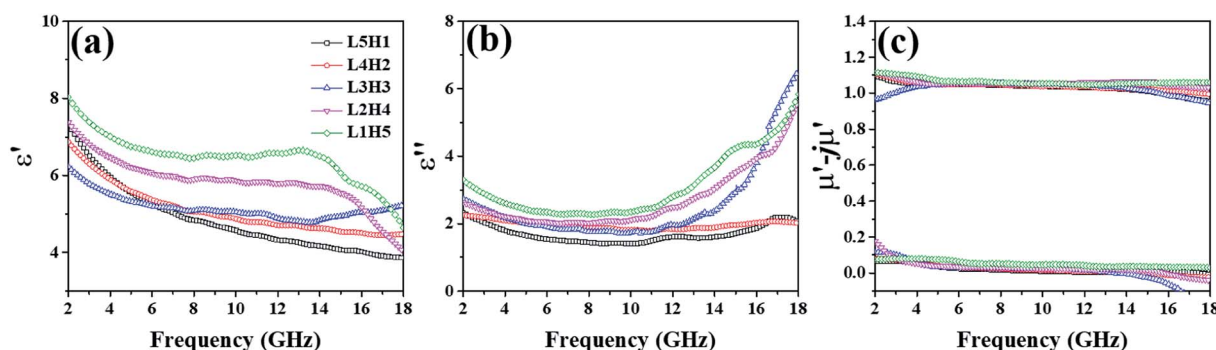

Fig. 8 Frequency dependent (a and b) complex permittivity ($\varepsilon_r = \varepsilon' − j\varepsilon''$) and (c) complex permeability ($\mu_r = \mu' − j\mu''$) of multi components stacking Fe$_3$Si/SiC fibers/silicon resin composite (5 wt%) samples.
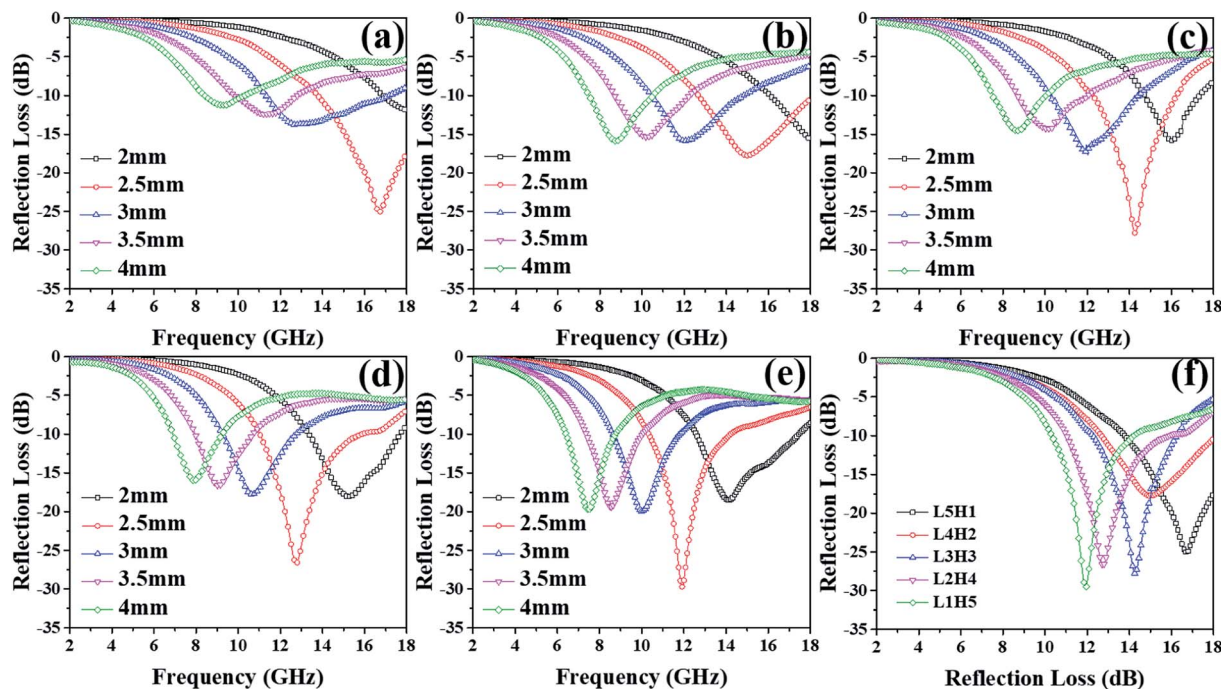
Fig. 9 Calculated frequency dependent reflection loss (RL) of multi components stacking Fe_3Si/SiC fibers/silicon resin composite (5 wt%) samples: (a) L5H1, (b) L4H2, (c) L3H3, (d) L2H4, (e) L1H5 and (f) RL peaks of all samples at the thickness of 2.5 mm.

Table 3 Comparison of microwave absorption properties of multi components stacking Fe_3Si/SiC fibers/silicon resin composite (5 wt%) samples

Samples	Minimal RL (dB)	Frequency of RL_{min} (GHz)	d_{min} (mm)	EAB (GHz) (RL < −10 dB)
L5H1	−25.4	16.7	2.5	6.3 (11.1–17.4)
L2H4	−18.1	15.0	2.5	5.5 (12.5–18.0)
L3H3	−28.2	14.3	2.5	4.4 (10.1–14.5)
L4H2	−26.9	12.8	2.5	5.5 (10.9–16.4)
L1H5	−30.1	11.9	2.5	5.2 (12.5–17.7)

The calculated reflection loss (RL) results of different multi components stacking fiber mats composites based on eqn (1)–(3) are shown in Fig. 9(a)–(e). And some key parameters are also compared in Table 3. Compared with Fe_3Si-1.6 wt% or Fe_3Si-6.3 wt% sample, all the multi components stacking fiber mats composites exhibit better microwave absorption properties. The enhanced RL values could be resulted from the suitable characteristic impedance matching degree as we have discussed in the 3.2.1 Section (see Fig. S4 and S5†). From Fig. 9(a)–(e) it could be seen that all the absorption bands shift to lower frequency range as more high Fe_3Si content layers stacked into the composite. And the RL peaks of all samples at the thickness of 2.5 mm were picked out and illustrated in Fig. 9(f), where the frequency of minimal RL value shifts from 16.7 to 11.9 GHz (see Table 3) as the high Fe_3Si content layer number gradually increases from 1 to 5. The remarkable shifting effect could be explained by the quarter-wavelength ($\lambda/4$) cancellation theory, which is widely accepted to investigate the relationship between absorption band frequency (f) and sample thickness (t_m) according to the following equation:[54–57]

$$t_m = nc/[(4f)(|\varepsilon_r||\mu_r|)^{1/2}] \quad (n = 1, 3, 5,\ldots) \quad (4)$$

Fig. S6† shows the frequency-dependent $\lambda/4$ and $3\lambda/4$ of the multi components stacking fiber mats composites. Apparently, both $\lambda/4$ and $3\lambda/4$ lines of L5H1 sample lie above the top, then followed by the sample of L4H2, L3H2, L2H4 and L1H5, respectively. Namely, with a specified sample thickness, the position of minimal RL peak would turn to the lower frequency range when more high Fe_3Si content layers are stacked into the composites. The conclusion from Fig. S6† quite agrees with the shifting effect of multi components stacking fiber mats composites, indicating that the microwave absorption band can also be manipulated by the designing of stacking component and structure.

4 Conclusions

We developed an effective method to fabricate flexible Fe_3Si/SiC ultrathin fiber mats with tunable EM and microwave absorption

properties by component and structure design. Fe(acac)$_3$ was selected as the Fe source in the PCS solution, which transformed into Fe$_3$Si phase in the Fe$_3$Si/SiC hybrid fibers. Compared with pure SiC fibers, the Fe$_3$Si/SiC hybrid fibers show smaller diameter of 1–2 μm. The flexibility of Fe$_3$Si/SiC hybrid fiber mats (Fe$_3$Si-1.6 and 3.8 wt%) are also greatly enhanced and remained undamaged after 500 times' 180° bending testing. Furthermore, the composition of Fe$_3$Si phase could bring improvement to the electrical conductivity and EM attenuation ability, associated with higher dielectric and magnetic loss. At the optimal Fe$_3$Si content of 3.8 wt%, the Fe$_3$Si/SiC fibers/silicon resin composite (5 wt%) could reach a minimal RL value of −22.5 dB at 16.5 GHz and 2.5 mm thickness with the EAB value as broad as 8.5 GHz. By varying the stacking structure of multi components stacking fiber mats composites, the microwave absorption performance can be further promoted and manipulated.

Conflicts of interest

There are no conflicts to declare.

Acknowledgements

Notes and references

1 X. Jin, X. Fan, C. Lu and T. Wang, *J. Eur. Ceram. Soc.*, 2018, **38**, 1–28.

2 R. Wu, K. Zhou, C. Y. Yue, J. Wei and Y. Pan, *Prog. Mater. Sci.*, 2015, **72**, 1–60.

3 M. Belmonte, *Adv. Eng. Mater.*, 2006, **8**, 693–703.

4 L. Su, H. Wang, M. Niu, X. Fan, M. Ma, Z. Shi and S.-W. Guo, *ACS Nano*, 2018, **12**, 3103–3111.

5 B. Sun, Y. Sun and C. Wang, *Small*, 2018, **14**, 1703391.

6 L. Cheng, Y. Xu, L. Zhang and X. Yin, *Composites, Part A*, 2000, **31**, 1015–1020.

7 X. Ma, X. Yin, X. Fan, X. Sun, L. Yang, F. Ye and L. Cheng, *J. Eur. Ceram. Soc.*, 2018, **38**, 1069–1078.

8 I. Spitsberg and J. Steibel, *Int. J. Appl. Ceram. Technol.*, 2004, **1**, 291–301.

9 R. Naslain, *Compos. Sci. Technol.*, 2004, **64**, 155–170.

10 Y. Katoh, K. Ozawa, C. Shih, T. Nozawa, R. J. Shinavski, A. Hasegawa and L. L. Snead, *J. Nucl. Mater.*, 2014, **448**, 448–476.

11 Y. Katoh, L. L. Snead, C. H. Henager, T. Nozawa, T. Hinoki, A. Iveković, S. Novak and S. G. De Vicente, *J. Nucl. Mater.*, 2014, **455**, 387–397.

12 M. Han, X. Yin, Z. Hou, C. Song, X. Li, L. Zhang and L. Cheng, *ACS Appl. Mater. Interfaces*, 2017, **9**, 11803–11810.

13 X. Yin, L. Kong, L. Zhang, L. Cheng, N. Travitzky and P. Greil, *Int. Mater. Rev.*, 2014, **59**, 326–355.

14 A. Mathur, S. B. Dutta, D. Pal, J. Singhal, A. Singh and S. Chattopadhyay, *Adv. Mater. Interfaces*, 2016, **3**, 1600413.

15 B. Wang, Y. Wang, Y. Lei, N. Wu, Y. Gou, C. Han, S. Xie and D. Fang, *Nano Res.*, 2016, **9**, 886–898.

16 A. Oliveros, A. Guiseppi-Elie and S. E. Saddow, *Biomed. Microdevices*, 2013, **15**, 353–368.

17 S. C. Chiu, H. C. Yu and Y. Y. Li, *J. Phys. Chem. C*, 2010, **114**, 1947–1952.

18 J. Kuang and W. Cao, *Appl. Phys. Lett.*, 2013, **103**, 112906.

19 J. Kuang, P. Jiang, W. Liu and W. Cao, *Appl. Phys. Lett.*, 2015, **106**, 212903.

20 S. Sarkar, J. Zou, J. Liu, C. Xu, L. An and L. Zhai, *ACS Appl. Mater. Interfaces*, 2010, **2**, 1150–1156.

21 L. P. Rajukumar, M. Belmonte, J. E. Slimak, A. L. Elías, E. Cruz-Silva, N. Perea-López, A. Morelos-Gómez, H. Terrones, M. Endo and P. Miranzo, *Adv. Funct. Mater.*, 2015, **25**, 4985–4993.

22 P. Wang, L. Cheng, Y. Zhang, H. Wu, Y. Hou, W. Yuan and L. Zheng, *Ceram. Int.*, 2017, **43**, 7424–7435.

23 Y. Cheng, M. Tan, P. Hu, X. Zhang, B. Sun, L. Yan, S. Zhou and W. Han, *Appl. Surf. Sci.*, 2018, **448**, 138–144.

24 X. Huang, X. Yan, L. Xia, P. Wang, Q. Wang, X. Zhang, B. Zhong, H. Zhao and G. Wen, *Scr. Mater.*, 2016, **120**, 107–111.

25 M. Sun, X. Lv, A. Xie, W. Jiang and F. Wu, *J. Mater. Chem. C*, 2016, **4**, 8897–8902.

26 J. Kuang, P. Jiang, F. Ran and W. Cao, *J. Alloys Compd.*, 2016, **687**, 227–231.

27 C. Liang, C. Liu, H. Wang, L. Wu, Z. Jiang, Y. Xu, B. Shen and Z. Wang, *J. Mater. Chem. A*, 2014, **2**, 16397–16402.

28 H. Wang, L. Wu, J. Jiao, J. Zhou, Y. Xu, H. Zhang, Z. Jiang, B. Shen and Z. Wang, *J. Mater. Chem. A*, 2015, **3**, 6517–6525.

29 Y. Hou, L. Cheng, Y. Zhang, Y. Yang, C. Deng, Z. Yang, Q. Chen, P. Wang and L. Zheng, *ACS Appl. Mater. Interfaces*, 2017, **9**, 7265–7271.

30 Y. Hou, L. Cheng, Y. Zhang, Y. Yang, C. Deng, Z. Yang, Q. Chen, X. Du and L. Zheng, *ACS Appl. Mater. Interfaces*, 2017, **9**, 43072–43080.

31 Y. Hou, B. Xiao, G. Yang, Z. Sun, W. Yang, S. Wu, X. Huang and G. Wen, *J. Mater. Chem. C*, 2018, **6**, 7661–7670.

32 X. Wang, B. Ding, G. Sun, M. Wang and J. Yu, *Prog. Mater. Sci.*, 2013, **58**, 1173–1243.

33 D. Li and Y. Xia, *Adv. Mater.*, 2004, **16**, 1151–1170.

34 D. Li, J. T. McCann, Y. Xia and M. Marquez, *J. Am. Ceram. Soc.*, 2006, **89**, 1861–1869.

35 P. Miles, W. Westphal and A. Von Hippel, *Rev. Mod. Phys.*, 1957, **29**, 279.

36 F. Ye, Q. Song, Z. Zhang, W. Li, S. Zhang, X. Yin, Y. Zhou, H. Tao, Y. Liu and L. Cheng, *Adv. Funct. Mater.*, 2018, 1707205.

37 L. Kong, C. Wang, X. Yin, X. Fan, W. Wang and J. Huang, *J. Mater. Chem. C*, 2017, **5**, 7479–7488.

38 K.-H. Chang and H.-L. Lin, *J. Polym. Res.*, 2009, **16**, 611–622.

39 N. A. M. Barakat, M. A. Kanjwal, F. A. Sheikh and H. Y. Kim, *Polymer*, 2009, **50**, 4389–4396.

40 M. M. Demir, I. Yilgor, E. Yilgor and B. Erman, *Polymer*, 2002, **43**, 3303–3309.

41 L. Wang, G. Wei, F. Gao, C. Li and W. Yang, *Nanoscale*, 2015, **7**, 7585–7592.

42 J. Thomas, J. Schumann, H. Vinzelberg, E. Arushanov, R. Engelhard, O. Schmidt and T. Gemming, *Nanotechnology*, 2009, **20**, 235604.

43 C. Deneke, J. Schumann, R. Engelhard, J. Thomas, C. Müller, M. Khatri, A. Malachias, M. Weisser, T. Metzger and O. Schmidt, *Nanotechnology*, 2008, **20**, 045703.

44 Y. Jing, S.-H. He and J.-P. Wang, *J. Nanopart. Res.*, 2013, **15**, 1517.

45 X. Sun, K. Sun, C. Chen, H. Sun and B. Cui, *Int. J. Mater. Chem.*, 2012, **2**, 218–224.

46 Z. Yu, L. Yang, H. Min, P. Zhang, C. Zhou and R. Riedel, *J. Mater. Chem. C*, 2014, **2**, 1057–1067.

47 C. Vakifahmetoglu, E. Pippel, J. Woltersdorf and P. Colombo, *J. Am. Ceram. Soc.*, 2010, **93**, 959–968.

48 Y. Kobayashi, T. Kaneko, M. Kamogawa, K. Asai, K. Akiyama and H. Funakubo, *J. Phys. D: Appl. Phys.*, 2007, **40**, 6873.

49 S.-C. Wong, A. Baji and S. Leng, *Polymer*, 2008, **49**, 4713–4722.

50 W. Duan, X. Yin, F. Ye, Q. Li, M. Han, X. Liu and Y. Cai, *J. Mater. Chem. C*, 2016, **4**, 5962–5969.

51 T. Wang, R. Han, G. Tan, J. Wei, L. Qiao and F. Li, *J. Appl. Phys.*, 2012, **112**, 104903.

52 Z. Li, G. Lin and L. Kong, *IEEE Trans. Magn.*, 2008, **44**, 2255–2261.

53 T. Zhang, J. Zhang, G. Wen, B. Zhong, L. Xia, X. Huang, H. Zhao, H. Wang and L. Qin, *Carbon*, 2018, **136**, 345–358.

54 B. Wang, J. Wei, Y. Yang, T. Wang and F. Li, *J. Magn. Magn. Mater.*, 2011, **323**, 1101–1103.

55 X. Li, H. Yi, J. Zhang, J. Feng, F. Li, D. Xue, H. Zhang, Y. Peng and N. J. Mellors, *J. Nanopart. Res.*, 2013, **15**, 1–11.

56 X. Li, J. Feng, Y. Du, J. Bai, H. Fan, H. Zhang, Y. Peng and F. Li, *J. Mater. Chem. A*, 2015, **3**, 5535–5546.

57 X. Yuan, L. Cheng and L. Zhang, *J. Alloys Compd.*, 2016, **680**, 604–611.